INTERNATIONAL JOURNAL FOR NUMERICAL METHODS IN FLUIDS, VOL. 20, 621–640 (1995)

FINITE VOLUME COMPUTATION OF INCOMPRESSIBLE TURBULENT FLOWS IN GENERAL CO-ORDINATES ON STAGGERED GRIDS

M. ZIJLEMA, A. SEGAL AND P. WESSELING

Faculty of Technical Mathematics and Informatics, Delft University of Technology, P.O. Box 5031, 2600 GA Delft, The Netherlands

SUMMARY

A brief review of the computation of incompressible turbulent flow in complex geometries is given. A 2D finite volume method for the calculation of turbulent flow in general curvilinear co-ordinates is described. This method is based on a staggered grid arrangement and the contravariant flux components are chosen as primitive variables. Turbulence is modelled either by the standard k–ε model or by a k–ε model based on RNG theory. Convection is approximated with central differences for the mean flow quantities and a TVD-type MUSCL scheme for the turbulence equations. The sensitivity of the method to the grid properties is investigated. An application of this method to a complex turbulent flow is presented. The results of computations are compared with experimental data and other numerical solutions and are found to be satisfactory.

KEY WORDS: finite volume; curvilinear co-ordinates; staggered grid; turbulent recirculating flow

1. INTRODUCTION

Solving incompressible turbulent flows using a boundary-fitted co-ordinate system is an important technique in CFD. It permits easy and accurate implementation of boundary conditions and makes the computation of flows in complex geometries possible. For this purpose two different approaches can be adopted. The first approach is a complete transformation of the Navier–Stokes equations to general co-ordinates. Such a co-ordinate-invariant formulation contains many geometric quantities and thus leads to more work and storage. Moreover, the equations involve Christoffel symbols, which may lead to inaccuracies on non-smooth grids. Another approach is a partial transformation, in which only the independent variables are transformed while retaining the velocity components as Cartesian components. As a result, the governing equations have a strong conservation form which has a much simpler structure and thus simplifies programming.

The choice of the two approaches mentioned above depends on the grid arrangement: staggered versus collocated. On staggered grids, Cartesian velocity components in general are not perpendicular to grid lines. Therefore this approach may lead to unstable discretization. Hence the choice of grid-oriented velocity components as dependent variables is preferable. On collocated grids, Cartesian velocity components as primitive variables in the momentum equations are satisfactory.

CCC 0271–2091/95/070621–20

Received 14 April 1994
Revised 24 July 1994

In order to compute turbulent flows, a turbulence model has to be chosen. Many investigators adopt isotropic eddy viscosity formulations, of which the k–ε model is the most prominent. This model consists of two transport equations for the turbulent kinetic energy k and its dissipation rate ε. Both equations contain a quantity P_k called the production rate of turbulent energy. In the co-ordinate-invariant approach this quantity contains Christoffel symbols (in 2D six different Christoffel symbols occur). Hence it seems attractive to implement the k–ε model with the Cartesian approach.

In the light of the above observations, the collocated/Cartesian approach for solving the Reynolds-averaged Navier–Stokes equations with the k–ε model has become very popular and has been widely used over the last 15 years.[1–14]

In the collocated approach the pseudocompressibility method can also be used. This has been done e.g. in References 15 and 16. The former used an algebraic eddy viscosity model while the latter used the k–ε model. The main disadvantage of this method is that for time-dependent flow problems it is difficult to obtain accurate mass conservation.

Although the collocated approach is very popular, an important disadvantage of this approach is that there are special measures required to obtain a stable discretization (e.g. the interpolation proposed in Reference 2 to avoid decoupling between pressure and velocity).

Staggered grid arrangement has important advantages for incompressible flow computations, because this arrangement avoids non-physical pressure oscillations. Some publications discretizing the Reynolds-averaged Navier–Stokes equations for staggered grids with Cartesian velocity components as primitive variables and including the k–ε model in general co-ordinates are References 17–20. As mentioned before, this approach may give rise to unstable discretizations. Following Chen *et al.*,[20] the more common way to avoid this is to choose the co-ordinate system such that the angle between the velocity components and the grid lines is not too large. However, for general domains it is very difficult to achieve this, especially in 3D.

Discretizations for staggered grids with grid-oriented velocity components as unknowns with the k–ε model are presented in References 21–26. Stern *et al.*[24] have formulated the governing equations in vector notation, which has the advantage that Christoffel symbols do not occur explicitly. Rastogi[22] and Majumdar and Rodi[25] use contravariant velocity components to solve the Navier–Stokes equations, while Pope,[21] Demirdzic *et al.*[23] and Koshizuka and Oka[26] employ contravariant physical velocity components as unknowns.

In References 27–29 a co-ordinate-invariant discretization of the incompressible Navier–Stokes equations on a general staggered grid has been developed. Standard tensor notation has been used. As a consequence, the formulation contains Christoffel symbols. In spite of that, discretization accuracy can be maintained if certain rules concerning the approximation of the geometric quantities are followed, the contravariant flux instead of velocity components are chosen as primitive variables and the grid is not too non-smooth. Good results are obtained for 2D laminar flows on fairly smooth grids.

At present it is hard to say which approach is best to compute incompressible flows in arbitrary geometries, but it is certainly not obvious that the collocated/Cartesian approach is to be preferred.

In this paper a finite volume method for turbulent flow predictions on staggered grids in complex geometries employing the contravariant flux components as dependent variables is presented. We will show that this approach works well even on moderately non-smooth grids. Turbulence is modelled either by the standard high-Re k–ε model with wall functions or by a k–ε model based on renormalization group theory recently derived by Yakhot *et al.*,[30] The discretization incorporates central differences for the momentum equations and a TVD formulation of the second-order upwind scheme obtained with the MUSCL method for the turbulence equations. First, a simple test problem has been solved in order to investigate the influence of certain grid properties, such as skewness and non-uniformity, on the present method. Secondly, the method is applied to a realistic engineering problem, namely turbulent flow over a sand dune.

2. EQUATIONS GOVERNING INCOMPRESSIBLE TURBULENT FLOWS IN GENERAL CO-ORDINATES

In order to formulate the equations governing turbulent flow in general co-ordinates, tensor notation will be used; for an introduction see Reference 31.

The physical domain with curved boundaries Ω is transformed to a rectangle G with the mapping

$$T: \mathbf{x} = \mathbf{x}(\boldsymbol{\xi}), \quad \mathbf{x} \in \Omega, \quad \boldsymbol{\xi} \in G. \tag{1}$$

Here $\mathbf{x}$ are Cartesian co-ordinates and $\boldsymbol{\xi}$ are boundary-conforming curvilinear co-ordinates. The mapping is assumed to be regular, i.e. the Jacobian of the transformation does not vanish. Covariant base vectors $\mathbf{a}_{(\alpha)}$, contravariant base vectors $\mathbf{a}^{(\alpha)}$ and covariant and contravariant metric tensors $g_{\alpha\beta}$ and $g^{\alpha\beta}$ are defined as

$$\mathbf{a}_{(\alpha)} = \frac{\partial \mathbf{x}}{\partial \xi^{\alpha}}, \qquad \mathbf{a}^{(\alpha)} = \frac{\partial \xi^{(\alpha)}}{\partial \mathbf{x}}, \qquad g_{\alpha\beta} = \mathbf{a}_{(\alpha)} \cdot \mathbf{a}_{(\beta)}, \qquad g^{\alpha\beta} = \mathbf{a}^{(\alpha)} \cdot \mathbf{a}^{(\beta)}. \tag{2}$$

The square root of the determinant of the covariant metric tensor, denoted by $\sqrt{g}$, equals the Jacobian of the transformation. The following formulae for covariant derivatives of tensors of rank zero, one and two respectively are used in this paper:

$$\phi_{,\alpha} = \frac{\partial \phi}{\partial \xi^{\alpha}}, \tag{3}$$

$$U^{\alpha}_{,\beta} = \frac{\partial U^{\alpha}}{\partial \xi^{\beta}} + \begin{Bmatrix} \alpha \\ \gamma\beta \end{Bmatrix} U^{\gamma}, \tag{4}$$

$$U^{\alpha}_{,\alpha} = \frac{1}{\sqrt{g}} \frac{\partial \sqrt{g} U^{\alpha}}{\partial \xi^{\alpha}}, \tag{5}$$

$$T^{\alpha\beta}_{,\beta} = \frac{1}{\sqrt{g}} \frac{\partial \sqrt{g} T^{\alpha\beta}}{\partial \xi^{\beta}} + \begin{Bmatrix} \alpha \\ \gamma\beta \end{Bmatrix} T^{\gamma\beta}, \tag{6}$$

where

$$\begin{Bmatrix} \alpha \\ \gamma\beta \end{Bmatrix} = \mathbf{a}^{(\alpha)} \cdot \frac{\partial \mathbf{a}_{(\beta)}}{\partial \xi^{\gamma}} = \frac{\partial \xi^{\alpha}}{\partial x^{\delta}} \cdot \frac{\partial^2 x^{\delta}}{\partial x^{\gamma} \partial \xi^{\beta}} = \begin{Bmatrix} \alpha \\ \beta\gamma \end{Bmatrix} \tag{7}$$

is the Christoffel symbol of the second kind. The summation convention holds for Greek indices.

Turbulent flow is governed by the continuity equation and the Reynolds-averaged Navier–Stokes equations. The Reynolds stresses are related to the mean rates of strain through the isotropic eddy viscosity ν_t, which is calculated by the k–ε-type models. The tensor formulation of these equations is given by

$$U^{\alpha}_{,\alpha} = 0, \tag{8}$$

$$\frac{\partial U^{\alpha}}{\partial t} + \left(U^{\alpha} U^{\beta}\right)_{,\beta} + \left(g^{\alpha\beta} p\right)_{,\beta} - \left((\nu + \nu_t)(g^{\alpha\gamma} U^{\beta}_{,\gamma} + g^{\beta\gamma} U^{\alpha}_{,\gamma})\right)_{,\beta} = F^{\alpha}, \tag{9}$$

$$\nu_t = c_{\mu} \frac{k^2}{\varepsilon}, \tag{10}$$

$$\frac{\partial k}{\partial t} + (U^\alpha k)_{,\alpha} - \left(\frac{\nu_t}{\sigma_k} g^{\alpha\beta} k_{,\beta}\right)_{,\alpha} = P_k - \varepsilon, \tag{11}$$

$$\frac{\partial \varepsilon}{\partial t} + (U^\alpha \varepsilon)_{,\alpha} - \left(\frac{\nu_t}{\sigma_\varepsilon} g^{\alpha\beta} \varepsilon_{,\beta}\right)_{,\alpha} = \frac{\varepsilon}{k}(c_{\varepsilon 1} P_k - c_{\varepsilon 2}\varepsilon), \tag{12}$$

where U^α is the contravariant mean velocity component, p is the pressure, ν is the kinematic viscosity, F^α is an external force per unit volume, k is the turbulent kinetic energy, ε is the turbulent energy dissipation rate and P_k is the production of turbulent energy, given by

$$P_k = \nu_t g_{\alpha\delta}(g^{\alpha\gamma} U^\beta_{,\gamma} + g^{\beta\gamma} U^\alpha_{,\gamma}) U^\delta_{,\beta}. \tag{13}$$

Equations (10)–(12) contain five constants c_μ, $c_{\varepsilon 1}$, $c_{\varepsilon 2}$, σ_k and σ_ε. In the standard k–ε model[32] these constants are obtained from experiments for local equilibrium shear layer and isotropic turbulence. Following Launder and Spalding,[32] their values are chosen as 0·09, 1·44, 1·92, 1·0 and 1·3 respectively. In the RNG-based k–ε model, derived by Yakhot and co-workers,[30,33] the constants are calculated explicitly by RNG theory and are given by $c_\mu = 0{\cdot}085$, $c_{\varepsilon 2} = 1{\cdot}68$, $\sigma_k = 0{\cdot}7179$ and

$$c_{\varepsilon 1} = 1{\cdot}42 - \frac{\eta(1 - \eta/\eta_0)}{1 + \beta\eta^3}, \quad \text{with } \eta = \sqrt{\left(\frac{P_k}{c_\mu \varepsilon}\right)}, \quad \eta_0 = 4{\cdot}38 \text{ and } \beta = 0{\cdot}012. \tag{14}$$

Specification of the boundary conditions is straightforward, except in near-wall regions where wall functions are adopted which use empirical laws to circumvent the inability of the k–ε model to predict a logarithmic velocity profile near a wall.[32] An important advantage of wall functions is that they allow the inclusion of empirical information for special cases, e.g. wall roughness. For a rough wall the wall shear stress τ_w is computed as follows:

$$\tau_w = \frac{c_\mu^{1/4} \kappa \sqrt{k_P}}{\ln(E_r Y_P / h_R)} \mathbf{u} \cdot \mathbf{t}_P \quad \text{if } h_R^+ \equiv \frac{c_\mu^{1/4} \sqrt{k_P} h_R}{\nu} > 11{\cdot}6. \tag{15}$$

Here the subscript P denotes the grid point in the centre of the wall-adjacent control volumes, which is assumed to be located in a log-law region, Y is the distance perpendicular to the wall, h_R denotes the average height of roughness elements, $\mathbf{u} \cdot \mathbf{t}$ is the tangential velocity along the wall, κ is the Von Karman constant (approximately equal to 0·4) and E_r is a roughness parameter. For a very rough wall $E_r \approx 30$, as recommended by Schlichting.[34] For $h_R^+ < 11{\cdot}6$ the wall is considered to be smooth. In that case, wall functions for a smooth wall, as explained in Reference 32, can be employed:

$$\tau_w = \frac{c_\mu^{1/4} \kappa \sqrt{k_P}}{\ln(E Y_P^+)} \mathbf{u} \cdot \mathbf{t}_P, \quad \text{with } Y_P^+ = \frac{c_\mu^{1/4} Y_P \sqrt{k_P}}{\nu} \text{ and } E = 9{\cdot}0. \tag{16}$$

The rapid variation in turbulence quantities also necessitates special measures in evaluating the production and dissipation rates of turbulent kinetic energy near the wall. The average production and dissipation rates used in the near-wall cells have the following form:

$$\bar{P}_k = \tau_w \frac{\mathbf{u} \cdot \mathbf{t}_P}{Y_P}, \tag{17}$$

$$\bar{\varepsilon} = \begin{cases} c_\mu^{3/4} k_P^{3/2} \dfrac{\ln(E Y_P^+)}{\kappa Y_P}, & h_R^+ < 11{\cdot}6, \\ c_\mu^{3/4} k_P^{3/2} \dfrac{\ln(E_r Y_P / h_R)}{\kappa Y_P}, & h_R^+ > 11{\cdot}6. \end{cases} \tag{18}$$

These replace P_k and ε respectively, which are source terms in the standard form of the equation for turbulent energy (11). Finally, the value of ε at the first grid point away from the wall is determined from

$$\varepsilon_{\mathrm{P}} = \frac{c_\mu^{3/4} k_{\mathrm{P}}^{3/2}}{\kappa Y_{\mathrm{P}}}. \tag{19}$$

3. DISCRETIZATION OF THE GOVERNING EQUATIONS

3.1. Invariant finite volume discretization

In discretizing the governing equations (8)–(12), the following requirements should be met for accuracy reasons.

1. The geometric identity $\oint a_\beta^{(\alpha)}\, \mathrm{d}\Gamma_\alpha = 0$ should be satisfied after discretization.
2. When representing a constant velocity field $\mathbf{u}$ in terms of its contravariant components U^α and recomputing $\mathbf{u}$ from U^α, the original vector field $\mathbf{u}$ should be recovered exactly.

The first requirement imposes rules on the approximation of geometric quantities. The second requirement can be met if the flux components $V^\alpha = \sqrt{g} U^\alpha$ are chosen as unknowns. More details can be found in References 27–29. A finite volume method is used to discretize the governing equations on a staggered grid in the computational rectangle G. In G we choose a uniform grid, selecting the mapping $\mathbf{x} = \mathbf{x}(\boldsymbol{\xi})$ such that the mesh size $\delta\xi^\alpha = 1$. Figure 1 shows the locations of the points for the velocities U^α and pressure p in the grid. The turbulence quantities k and ε are evaluated at pressure points. For brevity the momentum and k–ε equations are written in the following form:

$$T^{\alpha\beta}_{,\beta} = F^\alpha - \frac{\partial U^\alpha}{\partial t}, \tag{20}$$

where

$$T^{\alpha\beta} = U^\alpha U^\beta + g^{\alpha\beta} p - (\nu + \nu_{\mathrm{t}})\left(g^{\alpha\gamma} U^\beta_{,\gamma} + g^{\beta\gamma} U^\alpha_{,\gamma}\right), \tag{21}$$

and

$$Q^\alpha_{,\alpha} = S_\phi - \frac{\partial \phi}{\partial t}, \tag{22}$$

where

$$Q^\alpha = U^\alpha \phi - \frac{\nu_{\mathrm{t}}}{\sigma_\phi} g^{\alpha\beta} \phi_{,\beta}. \tag{23}$$

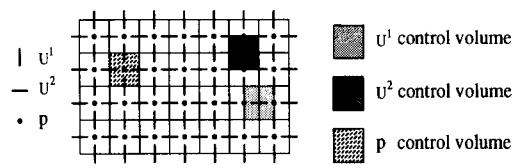

Figure 1. Arrangement of the unknowns for a staggered grid

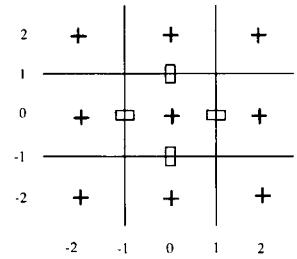

Figure 2. Local cell co-ordinates

Here $\phi = k$ or ε and S_ϕ represents the non-linear source terms. For convenience we introduce the local cell co-ordinates given by Figure 2.

Discretization of the continuity equation is obtained by integration over a finite volume Ω with centre (0, 0) using (5):

$$\int_\Omega U^\alpha_{,\alpha}\,\mathrm{d}\Omega = \int_\Omega \frac{\partial \sqrt{g}U^\alpha}{\partial \xi^\alpha}\mathrm{d}\xi^1\,\mathrm{d}\xi^2 \approx V^1\big|^{(1,0)}_{(-1,0)} + V^2\big|^{(0,1)}_{(0,-1)} = 0. \tag{24}$$

The momentum equation (20) is discretized in space as follows, taking for example a U^1-cell with centre at (1, 0), using (6):

$$\begin{aligned}\int_\Omega T^{1\beta}_{,\beta}\,\mathrm{d}\Omega &= \int_\Omega \frac{\partial \sqrt{g}T^{1\beta}}{\partial \xi^\beta}\mathrm{d}\xi^1\,\mathrm{d}\xi^2 + \int_\Omega \left\{\begin{matrix}1\\ \gamma\beta\end{matrix}\right\} T^{\gamma\beta}\sqrt{g}\,\mathrm{d}\xi^1\,\mathrm{d}\xi^2 \\ &\approx \sqrt{g}T^{11}\big|^{(2,0)}_{(0,0)} + \sqrt{g}T^{12}\big|^{(1,1)}_{(1,-1)} + \sqrt{g}\left\{\begin{matrix}1\\ \gamma\beta\end{matrix}\right\} T^{\gamma\beta}\big|_{(1,0)}.\end{aligned} \tag{25}$$

Integration of the momentum equation with $\alpha = 2$ over a U^2-cell with centre (0, 1) is done similarly.

Using (5), the transport equation (22) is integrated over a pressure cell with centre (0, 0), which yields

$$\int_\Omega Q^\alpha_{,\alpha}\,\mathrm{d}\Omega \approx \sqrt{g}Q^1\big|^{(1,0)}_{(-1,0)} + \sqrt{g}Q^2\big|^{(0,1)}_{(0,-1)}. \tag{26}$$

The right-hand sides of (20) and (22) are integrated using the midpoint rule:

$$\int_\Omega \left(F^\alpha - \frac{\partial U^\alpha}{\partial t}\right)\mathrm{d}\Omega \approx \sqrt{g}_{(k,l)}\left(F^\alpha - \frac{\partial U^\alpha}{\partial t}\right)\Big|_{(k,l)}, \tag{27}$$

$$\int_\Omega \left(S_\phi - \frac{\partial \phi}{\partial t}\right)\mathrm{d}\Omega \approx \sqrt{g}_{(0,0)}\left(S_\phi - \frac{\partial \phi}{\partial t}\right)\Big|_{(0,0)}, \tag{28}$$

with $(k, l) = (1, 0)$ if $\alpha = 1$ or $(k, l) = (0, 1)$ if $\alpha = 2$.

The discretization is completed by substituting (21) in (25) and (23) in (26). Furthermore, U^α is replaced by $V^\alpha/\sqrt{g}$.

The cell face fluxes containing cell face values (convection) and derivatives (diffusion) have to be approximated. In the case of the momentum equations only central differences combined with (four-point) bilinear interpolations will be employed. Although the central difference scheme is non-monotone, so that it can to give rise to unphysical oscillations, typically in the vicinity of steep gradients, this does not occur, even at high Reynolds number. In fact, when the equations in question are weakly non-linear and coupled, central difference schemes or other higher-order non-monotone

schemes produces accurate results. However, in strongly coupled/non-linear situations, 'wiggles' occur and tend to grow in an unbounded manner, which prevents the solutions from converging. This is the reason why the convective transport of turbulence quantities, occurring e.g. in k–ε-type models, has been approximated with first-order upwind schemes in numerous publications (e.g. References 2, 3, 9, 10, 17, 23 and 25). However, these schemes produce excessive numerical diffusion, particularly when the grid lines are not aligned with streamlines. Hence the use of higher-order schemes is essential when turbulence transport equations have to be accurately resolved but monotonicity must be ensured.

In the present paper a TVD/MUSCL scheme with the Chakravarthy–Osher limiter, commonly used in compressible Euler codes, is adapted for the accurate approximation of convective turbulence transport. Further details and an overview of TVD schemes can be found in Reference 35. Using a second-order upwind scheme obtained by means of van Leer's MUSCL approach,[36] the approximation of the face value ϕ at point (1, 0), for example, is given by

$$\phi_{(1,0)} = \phi_{(0,0)} + \tfrac{1}{4}[(1-\kappa)\Psi(\phi_{(0,0)} - \phi_{(-2,0)},\ \phi_{(2,0)} - \phi_{(0,0)}) + (1+\kappa)\Psi(\phi_{(2,0)} - \phi_{(0,0)},\ \phi_{(0,0)} - \phi_{(-2,0)})] \quad \text{if } V^1_{(1,0)} \geq 0, \tag{29}$$

$$\phi_{(1,0)} = \phi_{(2,0)} - \tfrac{1}{4}[(1-\kappa)\Psi(\phi_{(4,0)} - \phi_{(2,0)},\ \phi_{(2,0)} - \phi_{(0,0)}) + (1+\kappa)\Psi(\phi_{(2,0)} - \phi_{(0,0)},\ \phi_{(4,0)} - \phi_{(2,0)})] \quad \text{if } V^1_{(1,0)} < 0. \tag{30}$$

The parameter κ indicates a specified scheme; for instance, $\kappa = -1$ corresponds to the fully second-order one-sided upwind scheme. To avoid non-monotone behaviour of the solution, a limiter Ψ is introduced in the scheme (29), (30). Here the Chakravarthy–Osher limiter is chosen, defined by

$$\Psi(p,\ q) = \text{minmod}(p,\ \beta q) \equiv \text{sign}(p)\max\{0,\ \min[|p|,\ \beta q\ \text{sign}(p)]\}, \tag{31}$$

with $1 \leq \beta \leq (3-\kappa)/(1-\kappa)$ for all ratios of consecutive gradients $p/q \geq 0$. For simplicity we choose $\beta = 1$, i.e. equations (29) and (30) reduce to

$$\phi_{(1,0)} = \phi_{(0,0)} + \tfrac{1}{2}\,\text{minmod}(\phi_{(0,0)} - \phi_{(-2,0)},\ \phi_{(2,0)} - \phi_{(0,0)}) \quad \text{if } V^1_{(1,0)} \geq 0, \tag{32}$$

$$\phi_{(1,0)} = \phi_{(2,0)} - \tfrac{1}{2}\,\text{minmod}(\phi_{(4,0)} - \phi_{(2,0)},\ \phi_{(2,0)} - \phi_{(0,0)}) \quad \text{if } V^1_{(1,0)} < 0. \tag{33}$$

Because the limiter is non-linear, this TVD/MUSCL scheme is implemented in a deferred correction manner:

$$\phi^{n+1}_{(1,0)} = \phi^{U,n+1}_{(1,0)} + (\phi^{T,n}_{(1,0)} - \phi^{U,n}_{(1,0)}), \tag{34}$$

where n represents the time level and 'U' and 'T' indicate a first-order upwind and TVD/MUSCL scheme respectively. The first-order upwind scheme for the evaluation of ϕ at point (1, 0), for example, is given by

$$\phi_{(1,0)} = \tfrac{1}{2}\{1 + \text{sign}(V^1_{(1,0)})\}\phi_{(0,0)} + \tfrac{1}{2}\{1 - \text{sign}(V^1_{(1,0)})\}\phi_{(2,0)}. \tag{35}$$

Non-orthogonal co-ordinates introduce mixed derivatives in diffusion terms, which make the corresponding coefficient matrix not diagonally dominant. In some circumstances, e.g. when the grid is highly non-orthogonal, this scheme may produce numerical instability, especially when turbulence equations are involved. Many authors (e.g. References 2, 9 and 23) treat these derivatives in an explicit manner, i.e. calculate them from values obtained in the previous iteration, but this may cause deterioration of the convergence rate, especially when the mixed derivatives become large. For such cases another scheme proposed in Reference 37 may be employed, which is based on two-point rather

than four-point interpolation. For example, suppose that $g^{12} > 0$; then the following approximation is made:

$$\left.\frac{\partial \phi}{\partial \xi^2}\right|_{(1,0)} \approx \phi_{(1,1)} - \phi_{(1,-1)} = \tfrac{1}{2}(\phi_{(0,0)} + \phi_{(2,2)}) - \tfrac{1}{2}(\phi_{(0,-2)} + \phi_{(2,0)}). \tag{36}$$

Similarly, if $g^{12} < 0$,

$$\left.\frac{\partial \phi}{\partial \xi^2}\right|_{(1,0)} \approx \tfrac{1}{2}(\phi_{(0,2)} + \phi_{(2,0)} - \phi_{(0,0)} - \phi_{(2,-2)}). \tag{37}$$

It can be shown that this scheme guarantees boundedness of the solution, i.e. the coefficient matrix corresponding to the diffusion terms is diagonally dominant, if the following condition is satisfied:

$$|g^{12}| \leq \min(g^{11}, g^{22}). \tag{38}$$

The mixed derivatives are treated implicitly unless stated otherwise.

The discretization of the production of turbulent energy (13) is carried out by substituting (4) in (13) and with central differencing. Again U^α is replaced by $V^\alpha/\sqrt{g}$. In spite of the presence of Christoffel symbols, numerical experiments have shown that this discretization gives good results on reasonably smooth grids, as we will see.

The discretization of the V^1-momentum equation results in the 19-point stencil presented in Figure 3. The V^2-stencil is obtained by rotation over 90°. The total number of variables linked together in the transport equation is nine (cf. Figure 2).

Implementation of boundary conditions for the momentum and transport equations is discussed in References 29 and 38. Discussion of the implementation of periodic as well as antiperiodic boundary conditions in our code can be found in Reference 39.

3.2. *Time discretization and solution method*

The spatial discretization yields systems of ordinary differential equations of the following form:

$$D\mathbf{V} = \mathbf{0}, \tag{39}$$

$$\frac{\mathrm{d}\mathbf{V}}{\mathrm{d}t} + N(\mathbf{V}) + G\mathbf{P} = \mathbf{F}, \tag{39}$$

$$\frac{\mathrm{d}\boldsymbol{\phi}}{\mathrm{d}t} + T(\mathbf{V})\boldsymbol{\phi} = \mathbf{B} + \mathbf{S}_\phi, \tag{41}$$

where $\mathbf{V}$, $\mathbf{P}$ and ϕ denote algebraic vectors containing the velocity, pressure and scalar unknowns respectively. Furthermore, D and G are the discretized divergence and gradient operators respectively,

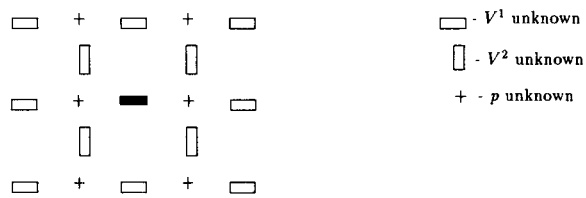

Figurer 3. Stencil for V^1-momentum equation

N and T represent the discretization of convection and diffusion terms respectively, $\mathbf{F}$ contains the discretized source term and boundary values, $\mathbf{B}$ represents a right-hand-side term arising from the boundary conditions and $\mathbf{S}_\phi$ contains the source term which is a function of $\mathbf{V}$ and $\boldsymbol{\phi}$. Time discretization takes place with the implicit Euler method. Linearization of non-linear terms is carried out with the standard Newton method:

$$N(\mathbf{V}^{n+1}) \approx N(\mathbf{V}^n) + \frac{\partial N^n}{\partial \mathbf{V}}(\mathbf{V}^{n+1} - \mathbf{V}^n), \tag{42}$$

$$\mathbf{S}_\phi^{n+1} \approx \mathbf{S}_\phi^n + \frac{\partial \mathbf{S}_\phi^n}{\partial \boldsymbol{\phi}}(\boldsymbol{\phi}^{n+1} - \boldsymbol{\phi}^n). \tag{43}$$

For both the k- and ε-equations the inequalities $\mathbf{S}_\phi^n \geq 0$ and $\partial \mathbf{S}_\phi^n / \partial \boldsymbol{\phi} < 0$ must hold, because these are sufficient but not necessary conditions to preserve positivity of k and ε. Assuming that v_t is frozen at time level n, then the dissipation term in equation (11) at time level $n+1$ is linearized as follows:

$$-\varepsilon^{n+1} \approx -c_\mu \frac{(k^{n+1})^2}{v_t^n} \approx -\frac{2c_\mu k^n}{v_t^n} k^{n+1} + c_\mu \frac{(k^n)^2}{v_t^n} = \varepsilon^n - 2\frac{\varepsilon^n}{k^n} k^{n+1}, \tag{44}$$

which satisfies the aforementioned inequalities. Note that P_k in equations (11) and (12) is non-negative.

The resulting systems of linear equations are solved by a Krylov subspace method of GMRES type[40] with preconditioning. This method is very suitable for non-symmetric matrices, has a relatively good rate of convergence and is vectorizable to a satisfactory degree. For more details we refer to Reference 41. Most authors[9,10,17,23,25] have adopted more slowly convergent iterative methods for solving the momentum and turbulence equations, of which the line Gauss–Seidel method and the strongly implicit method of Stone[42] are the most prominent. Both iterative methods are only partly vectorizable.

The overall solution algorithm can be summarized as follows. First, the continuity equation and the momentum equations are solved. To ensure a divergence-free velocity field, a second-order pressure correction method as described in Reference 43 is used. Details can be found e.g. in Reference 29. Finally, the equations for k and ε are solved in a decoupled way. Time stepping is repeated until a stationary solution is obtained.

4. RESULTS

The results presented in this section consist of two parts. The first part contains results for the turbulent flow through a straight channel, while the second part contains results for the turbulent flow over a sand dune. The numerical experiments for the flow in a channel were carried out to investigate the effects of non-orthogonality, non-smoothness and stretching of grid lines on the accuracy, stability and efficiency of the present method, especially when turbulence equations are involved. The flow over a sand dune was selected as an example of a flow problem, both geometrically and physically complex, for which experimental data are available.

4.1. Turbulent flow through a straight channel

The test problem is that of developing turbulent flow between two parallel plates with a length-to-width aspect ratio of 150. The Reynolds number based on inlet velocity and channel width H is $Re_H = 10^7$.

Owing to symmetry, only one half of the domain needs to be considered. Uniform inlet profiles were prescribed for all variables. In addition, wall functions, symmetry and outflow conditions (i.e. both tangential and normal stresses as well as normal gradients of turbulence quantities are zero) were employed. The computations were performed with four different grids, each consisting of 40×20 cells, as shown in Figure 4: a uniform grid, a stretched grid with a cell aspect ratio of 100, a moderately non-smooth grid and a skewed grid.

Figures 5 and 6 show the normalized velocity and normalized turbulent energy profiles respectively. Here $u_\tau = \sqrt{(\tau_w/\rho)}$ is the friction velocity, where τ_w is the wall shear stress. The location of the profiles is at $110H$ downstream from the entrance. Following Tennekes and Lumley,[44] the fully developed velocity profile for turbulent channel flow is expected to be logarithmic near the wall, whereas the dependence of the fully developed turbulent kinetic energy on the distance to the wall is assumed to be linear, as is indeed the case in Figures 5 and 6. Convergence towards steady state was in all cases stable, provided that in the skewness case the mixed derivatives in the turbulence equations were approximated according to (36) and (37). However, slower convergence was observed in cases of grid skewness and non-uniformity: the number of time steps needed to reach the converged solution was increased by up to 3%, 10% and 115% respectively in cases of non-smooth, stretched and skewed grids with respect to the uniform grid.

No effect of grid non-orthogonality and non-smoothness on accuracy was observed. However, in the velocity as well as the turbulent energy profiles, small discrepancies due to stretching of grid lines have been observed. No adverse effects attributable to the Christoffel symbols in the production term (13) were observed on the non-smooth grid. It should be noted that the uniform and skewed grids were insufficiently fine to resolve the steep velocity gradient near the wall.

No instabilities or wiggles were encountered in these calculations when convection in the momentum equations was approximated with central differences.

Based on the results discussed above, it appears that the present method is robust with respect to the grid skewness and non-uniformity, at least for the range of grids considered.

4.2. Turbulent flow over a sand dune

Description of the problem. The problem considered here is turbulent flow over a sand dune, which is a typical hydraulic flow problem. Earlier calculations related to this problem have been carried out e.g. by Perić *et al.*[45] The experimental data are taken from Reference 45 and are used here to assess the performance of the present method.

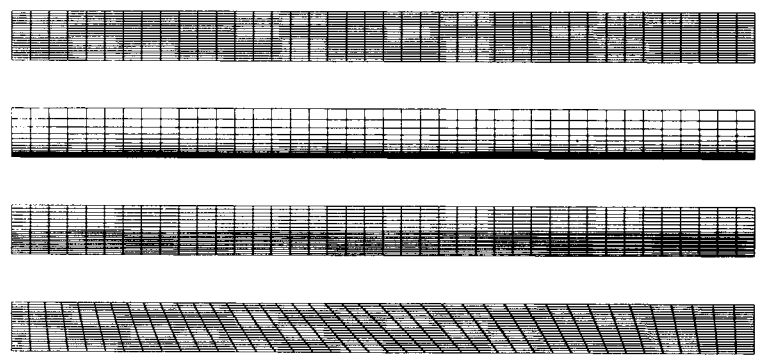

Figure 4. Four different grids: uniform, stretched, non-smooth and skewed (from top to bottom)

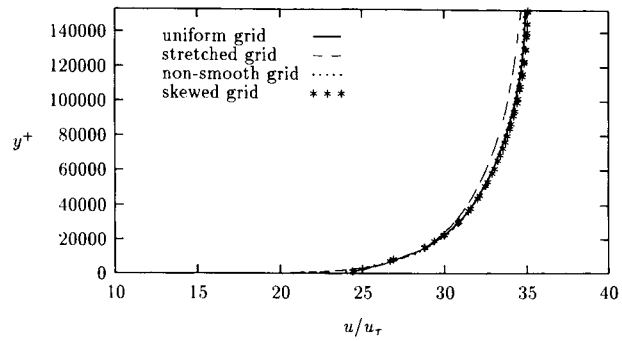

Figure 5. Streamwise velocity profiles at $x/H = 110$

The water flow configuration over a two-dimensional sand dune is presented in Figure 7. The average water depth is 0·3 m and the bulk inlet velocity is 0·43 m s^{-1}. Hence the Reynolds number is approximately 100,000. The bottom surface is covered with sand particles and the average roughness height is $1{\cdot}5 \times 10^{-3}$ m.

Boundary conditions. The inlet boundary conditions for the horizontal and vertical velocities and turbulent kinetic energy are prescribed according to the experimental data. The inlet dissipation of the turbulent energy is estimated from

$$\varepsilon_{\text{in}} = \frac{c_\mu^{3/4} k_{\text{in}}^{3/2}}{l}, \tag{45}$$

where the length scale l is given by

$$l = \min(\kappa y,\ 0{\cdot}1H) \tag{46}$$

and H is the inlet depth. At the outflow section it is assumed that the tangential and normal stresses and normal gradients of turbulence quantities are all zero. The free surface is treated as a symmetry line. As a consequence, the normal velocity and tangential stress are both zero and a zero-normal-gradient

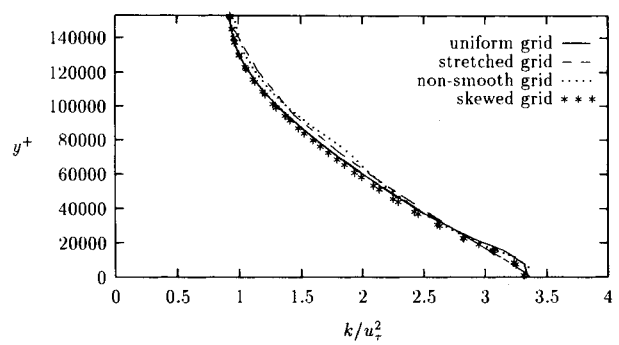

Figure 6. Turbulent kinetic energy profiles at $x/H = 110$

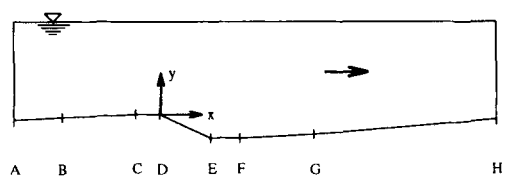

	x	y
A	-0.48	-0.019
B	-0.34	-0.008
C	-0.08	0.000
D	0.00	0.000
E	0.16	-0.083
F	0.26	-0.083
G	0.51	-0.072
H	1.12	-0.019

Figure 7. Geometry of the domain for the sand dune flow

condition is valid for turbulence quantities. Finally, in the wall region the wall functions for rough walls are used.

Grids and grid dependence test. Calculations using the standard k–ε model were performed with three different grids: 80 × 40, 120 × 60 and 160 × 80 cells. In Figure 8 the 80 × 40 grid is shown. The three grids have been refined in the vicinity of the wall to resolve steep gradients of flow properties.

The sensitivity of the numerical solutions to grid refinement is examined by comparing the predicted friction velocities u_τ, where $\tau_w \equiv \rho u_\tau |u_\tau|$, along the wall for each grid. The friction velocity is found to be one of the most sensitive quantities. The result is shown in Figure 9. It can be seen that the differences are relatively small, whereas the largest differences occur only around the reattachment point. the 160 × 80 grid results were therefore taken as acceptably grid-independent and are presented in further detail below. It should be noted that all three grid results agree well with the experimental data. Furthermore, these results resemble the results of Perić *et al.*[45] very well.

Performance of the present method. To give an impression of the performance of the present method, information on the computing times will be given. All calculations were performed on an HP 9000/735 workstation (100% scalar) and the CPU time has been measured in seconds.

The momentum and transport equations are solved with the GMRES method combined with an ILUD preconditioner, whereas the pressure system is solved with a Bi-CGSTAB method preconditioned by an ILU decomposition. The reason for this is that a considerable gain in CPU time can be obtained by solving the pressure equations with the Bi-CGSTAB method instead of GMRES. Further details on these iterative methods can be found in References 41 and 46. The GMRES or Bi-CGSTAB iteration process stops at each time step if the ratio of the residual norm to the initial residual norm $\|\mathbf{r}\|_2/\|\mathbf{r}_0\|_2 < tol$. In the present computations, $tol = 10^{-6}$ for the momentum and transport equations and $tol = 10^{-8}$ for the pressure equation.

Table I gives for the different grids the average CPU time for building the systems and solving the equations and the average number of iterations for each system of equations for one time step. Furthermore, on the 160 × 80 grid, approximately 1100 time steps with $\Delta t = 0{\cdot}01$ s were needed for the convergence to stationary solutions; this corresponds to approximately 3·5 h of CPU time on the HP 9000/735 workstation. The calculations for the 120 × 60 and 80 × 40 grids converged to steady state in about 515 time steps with $\Delta t = 0{\cdot}02$ s and 325 time steps with $\Delta t = 0{\cdot}03$ s respectively. These

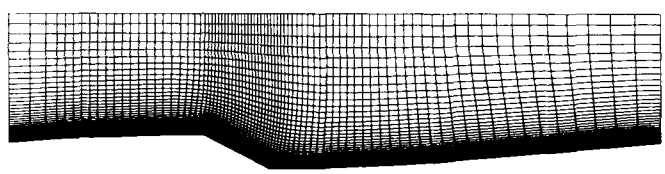

Figure 8. A typical grid for the sand dune flow (80 × 40 cells)

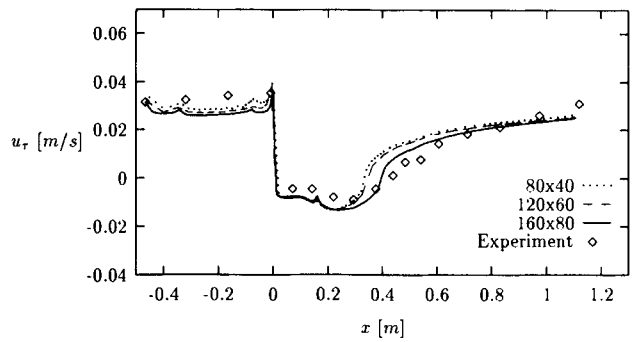

Figure 9. Grid dependence test

correspond to 50 and 10 min of CPU time respectively. The following conclusions can be drawn from Table I.

1. The solution (CPU) time per iteration tends to rise as N^{α}, where N is the number of grid cells and α varies from 1·20 to 1·26, which is typical for Krylov subspace methods.
2. The solution of the pressure equations is the most time-consuming part.
3. Building of the systems for turbulence equations is relative costly owing to the presence of the source terms.

It may be expected that for fine grid computations a large gain in CPU time can be obtained by taking coarse grid solutions instead of zero values as the initial guess. In this experiment the 80×40 grid is used to initiate the 160×80 grid computation. Furthermore, we use the Bi-CGSTAB method to solve the pressure equations. It appears that with $\Delta t = 0{\cdot}02$ s, typically 385 time steps were needed to obtain stationary solutions. The total CPU time was around 80 min on the HP. Hence a factor of approximately 2·5 is saved by taking coarse grid solutions instead of zero values as the initial guess for fine grid calculations.

Table I. Averaged CPU times (seconds) and number of iterations per time step using different grids

Grid	Equation	Building of systems	Solving the equations	Number of iterations
80×40	Momentum	0·19	0·52	12
	Pressure	0·02	0·59	23
	k	0·32	0·09	5
	ε	0·30	0·08	5
120×60	Momentum	0·38	1·49	13
	Pressure	0·07	1·82	26
	k	0·70	0·28	5
	ε	0·66	0·28	5
160×80	Momentum	0·67	2·24	9
	Pressure	0·13	4·95	34
	k	1·22	0·48	5
	ε	1·18	0·46	4

Predicted flow characteristics. Details of the predicted flow field features in the sand dune geometry are presented in Figures 10–13. They show clearly where separation and reattachment occur, the size and shape of the recirculation region and the pressure recovery after separation. Also evident are steep gradients of turbulent kinetic energy and length scales near the wall. The present streamlines and isobars patterns agree closely with those in Reference 45.

Comparison with experimental data. For comparison purposes, calculations are done with both standard and RNG-modified k–ε models. From the calculation with the RNG-based k–ε model on the 160×80 grid it turns out that the solutions typically needed about 1450 time steps ($\Delta t = 0{\cdot}01$ s) to converge to steady state and consumed about 4·5 CPU hours on the HP.

First we compare the predicted reattachment lengths for the different grids, turbulence models and convection schemes applied to the momentum equations with the measured one. These are summarized in Table II. The reattachment lengths computed by Peric′ *et al.*[45] are also included. They

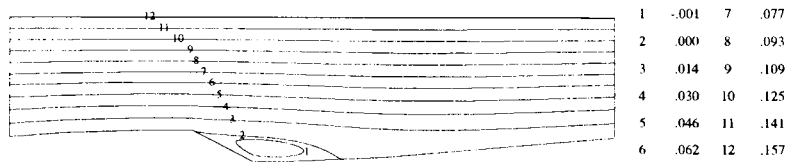

Figure 10. Streamlines for flow over sand dune

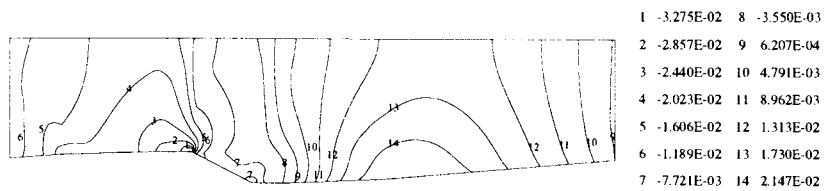

Figure 11. Isobars for flow over sand dune

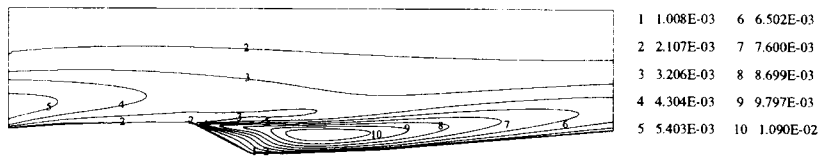

Figure 12. Turbulent kinetic energy pattern for flow over sand dune

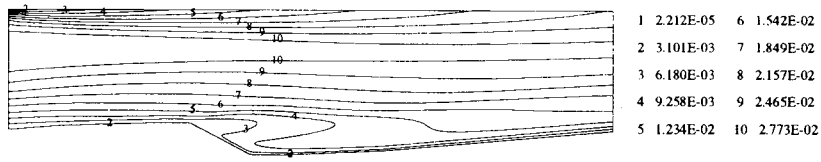

Figure 13. Isolines of length scales $c_\mu k^{3/2}/\varepsilon$ for flow over sand dune

Table II. Measured and predicted reattachment lengths using different grids, turbulence models and convection schemes for momentum

Case	Grid	Turbulence model	Convection scheme for momentum	Reattachment length (m)
Experiment	—	—	—	0·4245
Present	80 × 40	Standard k–ε	Central	0·3329
	120 × 60	Standard k–ε	Central	0·3490
	160 × 80	Standard k–ε	Central	0·4075
	160 × 80	RNG k–ε	Central	0·4738
Perić *et al.*[45]	80 × 40	Standard k–ε	Upwind	0·2867
	160 × 80	Standard k–ε	Upwind	0·3329
	160 × 80	Standard k–ε	Central	0·4372

used curvilinear non-orthogonal co-ordinates and a collocated grid in connection with Cartesian velocity components, whereas the convective turbulence transport has been approximated with the first-order upwind scheme. From this table it is seen that on the 160 × 80 grid the standard k–ε model slightly underpredicts the reattachment length, whereas the RNG-based k–ε model gives an overprediction of about 10%.

Detailed comparison of the predicted and experimental mean velocities (horizontal as well as vertical) is made in Figures 14–19. The locations of the cross-sections specified here are $x = -0{\cdot}02$ m (before separation), $x = 0{\cdot}21$ m (across the recirculation region) and $x = 0{\cdot}43$ m (just after reattachment). It can be observed that the calculations of the horizontal mean velocity with both standard and RNG-based k–ε models yield generally good agreement with the measurements for all the sections considered. Figure 16 indicates that the standard k–ε model underpredicts the reattachment length, while the RNG k–ε model overpredicts this length. Relatively large differences were obtained in the vertical mean velocity profiles.

Moreover, the predicted vertical velocity at $x = -0{\cdot}02$ m is contradictory to the measured one. It is believed that this must be attributed either to shortcomings of the turbulence models or to possible experimental errors. It is seen that the RNG k–ε model produces results in better agreement with the measurements than the standard k–ε model, especially close to the wall.

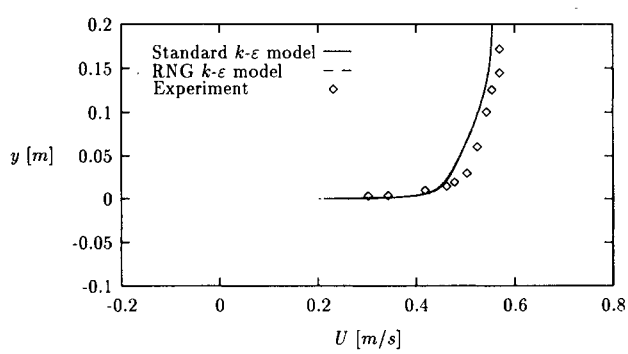

Figure 14. Horizontal velocity profile at $x = -0{\cdot}02$ m

The turbulent kinetic energy predictions are shown in Figures 20–22. Although the profile shapes are qualitatively similar, these profiles display an underprediction of turbulent energy surrounding and inside the recirculation region. This is a known defect of the k–ε-type models. However, the locations of local maxima are well predicted, especially by the RNG k–ε model. Furthermore, Figures 21 and 22 indicate that the standard k–ε model produces the best prediction of turbulent energy.

In Figure 23 the predicted variation in the water depth ζ, which is calculated using the hydrostatic pressure assumption, is compared with measurements. The qualitative agreement between prediction and measurements seems good.

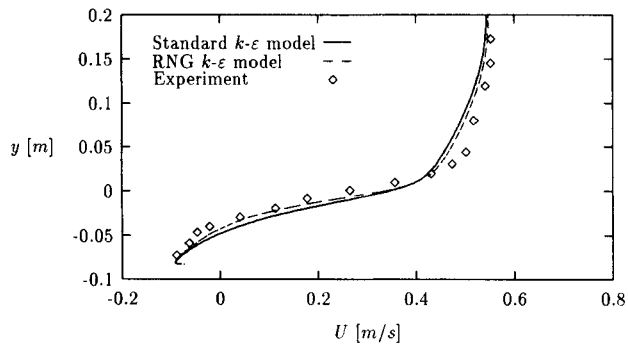

Figure 15. Horizontal velocity profile at x = 0·21 m

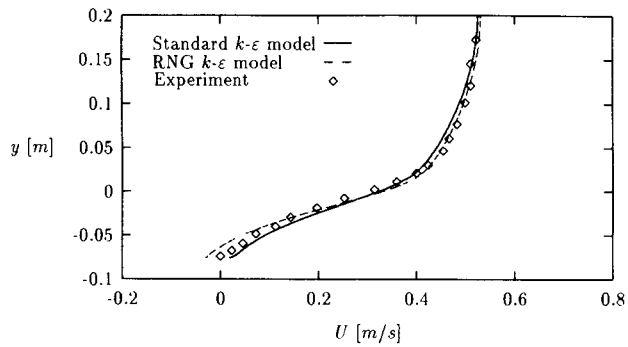

Figure 16. Horizontal velocity profile at x = 0·43 m

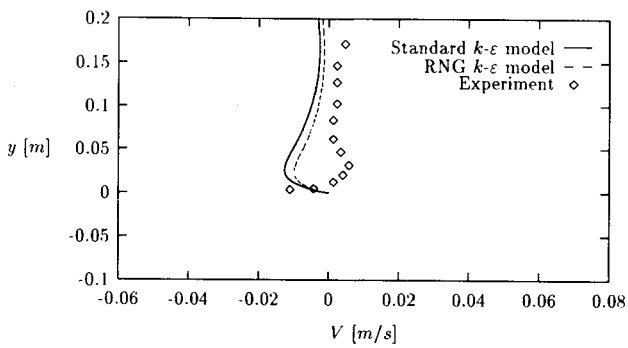

Figure 17. Vertical velocity profile at x = −0·02 m

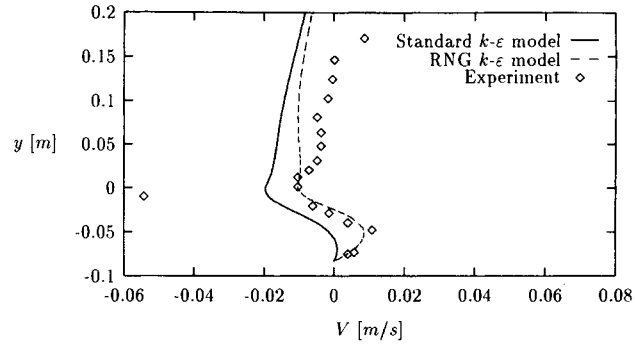

Figure 18. Vertical velocity profile at $x = 0{\cdot}21$ m

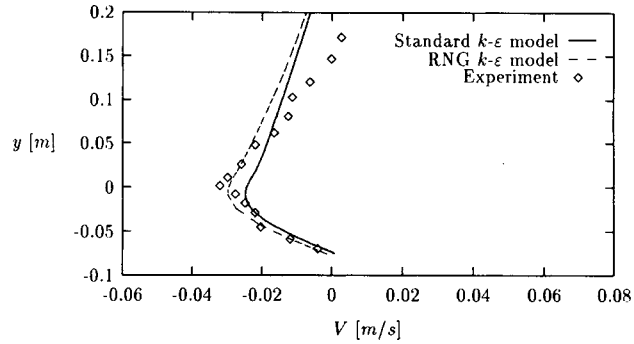

Figure 19. Vertical velocity profile at $x = 0{\cdot}43$ m

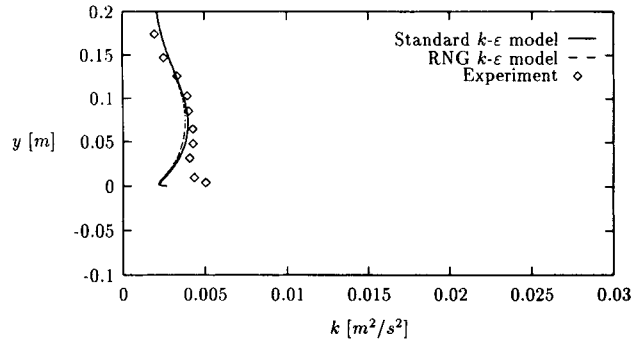

Figure 20. Turbulent kinetic energy at $x = -0{\cdot}02$ m

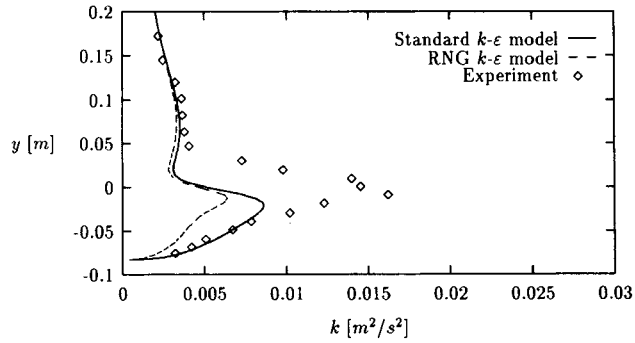

Figure 21. Turbulent kinetic energy at $x = 0{\cdot}21$ m

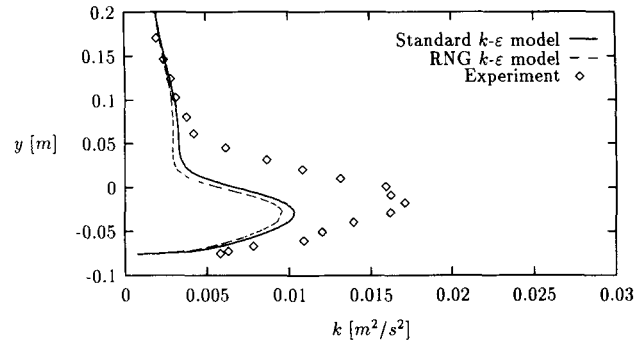

Figure 22. Turbulent kinetic energy at $x = 0{\cdot}43$ m

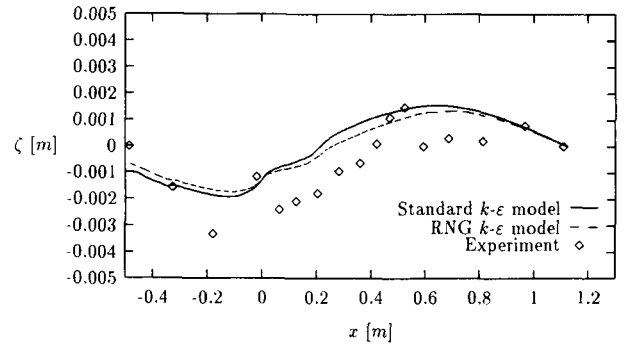

Figure 23. Variation in water depth

5. CONCLUSIONS

An invariant finite volume discretization in general co-ordinates of the Reynolds-averaged Navier–Stokes equations with the standard and RNG-modified k–ε models on staggered grids has been presented. Computational examples have shown that the staggered/invariant approach to computing turbulent flows also works well even on moderately non-smooth grids. The use of central differences to approximate the convection of volume fluxes offers good accuracy and no instability was encountered in spite of high Reynolds numbers. The TVD formulation of a second-order MUSCL scheme is employed for convection of k and ε to prevent negative values of k and ε and thus instability. The diffusion terms are approximated with central differences. The mixed derivatives in these terms are treated implicitly, except in highly non-orthogonal cases where the mixed derivatives are approximated according to (36) and (37). This does not affect the stability of the solution method, but it was found that this treatment lowers the convergence rate.

The present method was first assessed by applying it to a simple test case, namely turbulent flow through a straight channel for which the solution is known. It was found that no differences were observed between the solutions obtained on the skewed and fairly non-smooth grids and the uniform one. Only the accuracy of the solution of streamwise velocity and turbulent energy is affected a little by stretching of grid lines in which the mesh aspect ratio is relatively high. Finally, the present method was applied to turbulent flow over a 2D sand dune. This test case shows that both standard and RNG-based k–ε models produce satisfactory predictions of the mean flow field but represent the turbulent characteristics only in a qualitatively sense. Furthermore, the calculations are in accordance with earlier numerical results.

The efficiency and robustness of the present method are satisfactory. In the case of fine grid calculations, much CPU time can be saved by taking coarse grid solutions instead of zero values as the initial guess.

It is expected that the present method will produce inaccurate solutions when highly non-smooth grids are employed. An extension to the non-smooth case is currently being investigated by van Beek and Wesseling[47] and the results seem to be very promising. Extension to three-dimensional cases is also under consideration.

REFERENCES

1. M. A. Habib and J. H. Whitelaw, 'The calculation of turbulent flow in wide-angle diffusers', *Numer. Heat Transfer*, **5**, 145–164 (1982).
2. C. M. Rhie and W. L. Chow, 'Numerical study of the turbulent flow past an airfoil with trailing edge separation', *AIAA J.*, **21**, 1525–1532 (1983).
3. M. Perić, 'Finite volume method for the prediction of three- dimensional fluid flow in complex ducts', *Ph.D. Thesis*, Imperial College, London, 1985.
4. H. C. Chen and V. C. Patel, 'The flow around wing–body junctions', *Proc. Fourth Symp. on Numerical and Physical Aspects of Aerodynamic Fluids*, Long Beach, CA, 1989, pp. 1–15.
5. G. B. Deng, 'Numerical simulation of incompressible turbulent appendage–flat plate junction flows', in C. Taylor, W. G. Habashi and M. M. Hafez (eds), *Proc. Sixth Int. Conf. on Numerical Methods in Laminar and Turbulent Flows*, Pineridge, Swansea, 1989, pp. 793–803.
6. F.-S. Lien and M. A. Leschziner, 'Multigrid convergence acceleration for complex flow including turbulence', in W. Hackbush and U. Trottenberg (eds), *Multigrid Methods III*, Vol. 98, Birkhäuser, Basel, 1991, pp. 277–288.
7. J. Piquet and P. Queutey, 'Computation of the viscous flow past a prolate spheroid at incidence', in P. Wesseling (ed.), *Notes on Numerical Fluid Mechanics*, 29, *Proc. Eighth GAMM Conf. on Numerical Methods in Fluid Mechanics*, Vieweg, Braunschweig, 1990, pp. 464–474.
8. N.-H. Cho and C. A. J. Fletcher, 'Computation of turbulent conical diffuser flows using a non-orthogonal grid system', *Comput. Fluids*, **19**, 347–361 (1991).
9. M. C. Melaaen, 'Analysis of fluid flow in constricted tubes and ducts using body-fitted non-staggered grids', *Int. J. Numer. Methods Fluids*, **15**, 895–923 (1991).
10. P. J. Coelho and J. C. F. Pereira, 'Finite volume computation of the turbulent flow over a hill employing 2D or 3D non-orthogonal collocated grid systems', *Int. J. Numer. Methods Fluids*, **14**, 423–441 (1992).
11. J. Zhu and W. Rodi, 'Computation of axisymmetric confined jets in a diffuser', *Int. J. Numer. Methods Fluids*, **14**, 241–251 (1992).
12. Z. G. Xu, D. H. T. Gotham and M. W. Collins, 'Numerical modelling of three-dimensional turbulent flow in packaged air-conditioning units with inclined heat exchangers', in C. Taylor (ed.), *Proc. Eighth Int. Conf. on Numerical Methods in Laminar and Turbulent Flow*, Pineridge, Swansea, 1993, pp. 328–337.
13. H. Rolfes, J. A. Visser and A. Bekker, 'Simulation of wind flow over arbitrary shaped buildings', in C. Taylor (ed.), *Proc. Eighth Int. Conf. on Numerical Methods in Laminar and Turbulent Flow*, Pineridge, Swansea, 1993, pp. 643–654.
14. R. I. Issa and P. J. Oliveira, 'Numerical prediction of phase separation in two-phase flow through T-junctions', *Comput. Fluids*, **23**, 347–372 (1994).
15. D. Kwak, J. L. C. Chang, S. P. Shanks and S. R. Chakravarthy, 'A three-dimensional incompressible Navier–Stokes flow solver using primitive variables', *AIAA J.*, **24**, 390–396 (1986).
16. V. Michelassi and F. Martelli, 'Efficient solution of turbulent incompressible separated flows', in P. Wesseling (ed.), *Notes on Numerical Fluid Mechanics*, Vol. 29, *Proc. Eighth GAMM Conf. on Numerical Methods in Fluid Mechanics*, Vieweg, Braunschweig, 1990, pp. 373–390.
17. C. W. Rapley, 'Turbulent flow in a duct with cusped corners', *Int. J. Numer. Methods Fluids*, **5**, 155–167 (1985).
18. M. Braaten and W. Shyy, 'A study of recirculating flow computation using body-fitted coordinates: consistency aspects and mesh skewness', *Numer. Heat Transfer*, **9**, 559–574 (1986).
19. C.-N. Yung, T. G. Keith Jr. and K. J. de Witt, 'Numerical simulation of axisymmetric turbulent flow in combustors and diffusers', *Int. J. Numer. Methods Fluids*, **9**, 167–183 (1989).
20. H. C. Chen, V. C. Patel and S. Ju, 'Solutions of Reynolds-averaged Navier–Stokes equations for three-dimensional incompressible flows', *J. Comput. Phys.*, **88**, 305–336 (1990).
21. S. B. Pope, 'The calculation of turbulent recirculating flows in general orthogonal coordinates', *J. Comput. Phys.*, **26**, 197–217 (1978).
22. A. K. Rastogi, 'Hydrodynamics in tubes perturbed by curvilinear obstructions', *ASME J. Fluids Eng.*, **106**, 262–269 (1984).
23. I. Demirdzic, A. D. Gosman, R. I. Issa and M. Perić, 'A calculation procedure for turbulent flow in complex geometries', *Comput. Fluids*, **15**, 251–273 (1987).
24. F. Stern, S. Y. Yoo and V. C. Patel, 'Interactive and large-domain solutions of higher-order viscous-flow equations', *AIAA J.*, **26**, 1052–1060 (1988).

25. S. Majumdar and W. Rodi, 'Three-dimensional computation of flow past cylindrical structures and model cooling towers', *Build. Environ.*, **24**, 3–22 (1989).
26. S. Koshizuka and Y. Oka, 'A calculation procedure of coordinate-free Navier–Stokes equations on boundary-fitted grids, in C. Taylor, J. H. Chin and G. M. Homsy (eds), *Proc. Seventh Int. Conf. on Numerical Methods in Laminar and Turbulent Flow*, Pineridge, Swansea, 1991, pp. 1474–1484.
27. A. E. Mynett, P. Wesseling, A. Segal and C. G. M. Kassels, 'The ISNaS incompressible Navier–Stokes solver: invariant discretization', *Appl. Sci. Res.*, **48**, 175–191 (1991).
28. P. Wesseling, A. Segal, J. J. I. M. van Kan, C. W. Oosterlee and C. G. M. Kassels, 'Finite volume discretization of the incompressible Navier–Stokes equations in general coordinates on staggered grids', *Comput. Fluid Dyn. J.*, **1**, 27–33 (1992).
29. A. Segal, P. Wesseling, J. van Kan, C. W. Oosterlee and K. Kassels, 'Invariant discretization of the incompressible Navier–Stokes equations in boundary fitted co-ordinates', *Int. J. Numer. Methods Fluids*, **15**, 411–426 (1992).
30. V. Yakhot, S. A. Orszag, S. Thangam, T. B. Gatski and C. G. Speziale, 'Development of turbulence models for shear flows by a double expansion technique', *Phys. Fluids A*, **4**, 1510–1520 (1992).
31. R. Aris, *Vectors, Tensors and the Basic Equations of Fluid Mechanics*, Prentice-Hall, Englewood Cliffs, NJ, 1962.
32. B. E. Launder and D. B. Spalding, 'The numerical computation of turbulent flows', *Comput. Methods Appl. Mech. Eng.*, **3**, 269–289 (1974).
33. V. Yakhot and S. A. Orszag, 'Renormalization group analysis of turbulence. I. Basic theory', *J. Sci. Comput.*, **1**, 3–51 (1986).
34. H. Schlichting, *Boundary Layer Theory*, McGraw-Hill, New York, 1969.
35. C. Hirsch, *Numerical Computation of Internal and External Flows*, Vols 1 and 2, Wiley, Chichester, 1990.
36. B. van Leer, 'Towards the ultimate conservative difference scheme. V. A second-order sequel to Godunov's method', *J. Comput. Phys.*, **32**, 101–136 (1979).
37. I. A. Demirdzic, 'A finite volume method for computation of fluid flow in complex geometries', *Ph.D. Thesis*, University of London, 1982.
38. M. Zijlema, A. Segal and P. Wesseling, 'Invariant discretization of the k–ε model in general co-ordinates for prediction of turbulent flow in complicated geometries', *Comput. Fluids*, submitted.
39. G. Segal, K. Vuik and K. Kassels, 'On the implementation of symmetric and antisymmetric periodic boundary conditions for incompressible flow', *Int. J. Numer. Methods Fluids*, **18**, 1153–1165 (1994).
40. Y. Saad and M. H. Schultz, 'GMRES: a generalized minimal residual algorithm for solving non-symmetric linear systems', *SIAM J. Sci. Stat. Comput.*, **7**, 856–869 (1986).
41. C. Vuik, 'Solution of the discretized incompressible Navier–Stokes equations with the GMRES method', *Int. J. Numer. Methods Fluids*, **16**, 507–523 (1993).
42. H. L. Stone, 'Iterative solution of implicit approximations of multidimensional partial differential equations', *SIAM J. Numer. Anal.*, **5**, 530–558 (1968).
43. J. J. I. M. van Kan, 'A second-order accurate pressure correction method for viscous incompressible flow', *SIAM J. Sci. Stat. Comput.*, **7**, 870–891 (1986).
44. H. Tennekes and J. L. Lumley, *A First Course in Turbulence*, MIT Press, Cambridge, MA, 1983.
45. M. Perić, M. Rüger and G. Scheuerer, 'Calculation of the two- dimensional turbulent flow over a sand dune model', *Report SRR-TN-88- 02*, University of Erlangen–Nurnberg, 1988.
46. H. A. van der Vorst, 'Bi-CGSTAB: a fast and smoothly converging variant of Bi-CG for the solution of non-symmetric linear systems', *SIAM J. Sci. Stat. Comput.*, **13**, 631–644 (1992).
47. P. C. W. van Beek and P. Wesseling, 'Finite volume discretization of the incompressible Navier–Stokes equations in non-smooth boundary-fitted coordinates in two dimensions', *Report 93-57*, Faculty of Technical Mathematics and Informatics, Delft University of Technology, 1993.